



Peer review status:

This is a non-peer-reviewed preprint submitted to EarthArXiv.

# Statistical rock physics inversion for assessing source rock properties from seismic signatures: an application to the Canning Basin, Australia

Jiayuan Huang<sup>a\*</sup>, Allegra Hosford Scheirer<sup>b</sup>, Tapan Mukerji<sup>a,b,c</sup>

<sup>a</sup> *Department of Energy Science & Engineering, Stanford University, Stanford, California, USA*

<sup>b</sup> *Department of Earth & Planetary Sciences, Stanford University, Stanford, California, USA*

<sup>c</sup> *Department of Geophysics, Stanford University, Stanford, California, USA*

\**jiayuanh@stanford.edu*

## Abstract

Quantifying petrophysical properties and potentials of source rocks is important for subsurface modeling and characterization. However, predicting these properties using seismic signatures and well-log information is a high-dimensional, nonlinear inverse problem, and is subject to uncertainty due to data ambiguities. In this study, a statistical rock physics inversion workflow is proposed to efficiently estimate source rock properties and quantify their uncertainty from seismic signatures. A thermal maturation dependent elastic rock physics model is implemented to link source rock properties with elastic properties by Monte Carlo calibration. Statistical rock physics inversion based on weighted Approximate Bayesian Computation (ABC) is proposed to combine prior information from petrophysical knowledge, rock physics model calibration error, measured elastic properties data from well log and seismic data to estimate posterior distributions of source rock properties efficiently.

**Keywords:** Statistical inversion; Approximate Bayesian Computation (ABC); Uncertainty quantification; Rock physics modeling; Unconventional shale; Source rock properties; Canning Basin

## 1. Introduction

Understanding petrophysical properties such as porosity, total organic carbon (TOC), mineral composition, and fluid saturation is fundamental to the exploration and production of hydrocarbons. These properties play a crucial role in reservoir characterization, basin modeling, and production forecasting in petroleum industry (Clarkson, 2013; Mukerji et al., 2001; Peters et al., 2017). Rock physics models serve as the bridge between petrophysical properties and elastic properties, enabling geoscientists to predict subsurface properties from remote geophysical measurement (Mavko et al., 2020). Various rock physics models, such as the Gassmann fluid substitution model (Gassmann, 1951), Hertz-Mindlin contact theory (Hertz, 1882; Mindlin, 1949), inclusion models using self-consistent approximation and differential effective medium (DEM) theory (Berryman, 1995), have been developed and widely applied to different geological scenarios, each offering specific strengths depending on the complexity of the reservoir condition and data availability.

For non-linear rock physics models, it is difficult to obtain the analytical formulation to estimate petrophysical properties from elastic properties. Moreover, the rock physics models are often non-unique mappings from petrophysical properties to elastic properties, i.e., different combinations of petrophysical properties might give rise to very similar elastic properties. To address this problem, various rock physics inversion methods have been widely employed. These methods

range from deterministic techniques that optimize an objective function to stochastic frameworks that incorporate uncertainty in both data and models. Estimating subsurface properties from geophysical measurements is inherently uncertain due to data errors and model approximations (Bosch et al., 2010). Therefore, stochastic approaches are more practical for quantifying uncertainty for risk analysis and optimal decision-making (Grana et al., 2022).

Approximate Bayesian Computation (ABC) has gained attention for its flexibility and efficiency, particularly in cases where explicit likelihood functions are difficult to define (Rubin, 1984). In geophysics, and specifically in rock physics inversion, complex forward models and uncertain data distributions often make traditional Bayesian inference intractable. ABC circumvents the need for explicit likelihood evaluation by relying on simulations and summary statistics to approximate posterior distributions, making it particularly suitable for high-dimensional and nonlinear problems. This approach is adopted in subsurface characterization in this study, where it enables probabilistic assessment of rock properties while accounting for observational noise and modeling uncertainties.

In this study, we propose a novel rock physics inversion workflow based on weighted Approximate Bayesian Computation (ABC) to estimate petrophysical properties from elastic properties. The workflow begins with constructing a rock physics model tailored to the geological setting of the study area, followed by Monte Carlo sampling of mineral properties to calibrate the model using well-log data. To enhance inversion reliability, model calibration errors and data correlations are incorporated as weights into the ABC acceptance criteria. The weighted ABC framework is then employed to infer the posterior distribution of petrophysical properties by comparing simulated and observed elastic properties. We first do a sensitivity analysis of the rock physics model and test the workflow with a synthetic dataset. Then, we apply the proposed workflow to an unconventional shale formation in the Canning Basin, Australia, using well-log and seismically derived elastic properties. The results demonstrate the efficacy of weighted ABC in improving subsurface characterization and uncertainty quantification. The methods are described in the following section 2. This is followed by a Monte Carlo sensitivity analysis (section 3) and test with synthetic data (section 4). Section 5 finally presents the field application, followed by discussion and conclusions in section 6.

## **2. Methods**

### **2.1 Proposed workflow**

The goal of the proposed workflow is to quantify uncertainty of source rock properties, such as vitrinite reflectance, porosity, and kerogen content in unconventional shale reservoir from elastic properties, such as P- and S-wave velocities and impedances. In our workflow (Figure 1), Basin and Petroleum System Modeling (BPSM) is applied to simulate vitrinite reflectance, transformation ratio, and fluid saturation conditioned on basin geohistory and stratigraphy. The simulated vitrinite reflectance, transformation ratio, and fluid saturation can be used as priors for rock physics model inputs used for the inversion. Well logs are utilized to construct and calibrate the rock physics model and estimate prior distributions of kerogen, porosity, mineral, and fluid compositions. Finally, Approximate Bayesian computation (ABC) is applied to invert the rock physics model using elastic properties obtained from either well logs or seismic inversions to

estimate posterior distributions of vitrinite reflectance, kerogen, porosity, mineral, and fluid compositions.

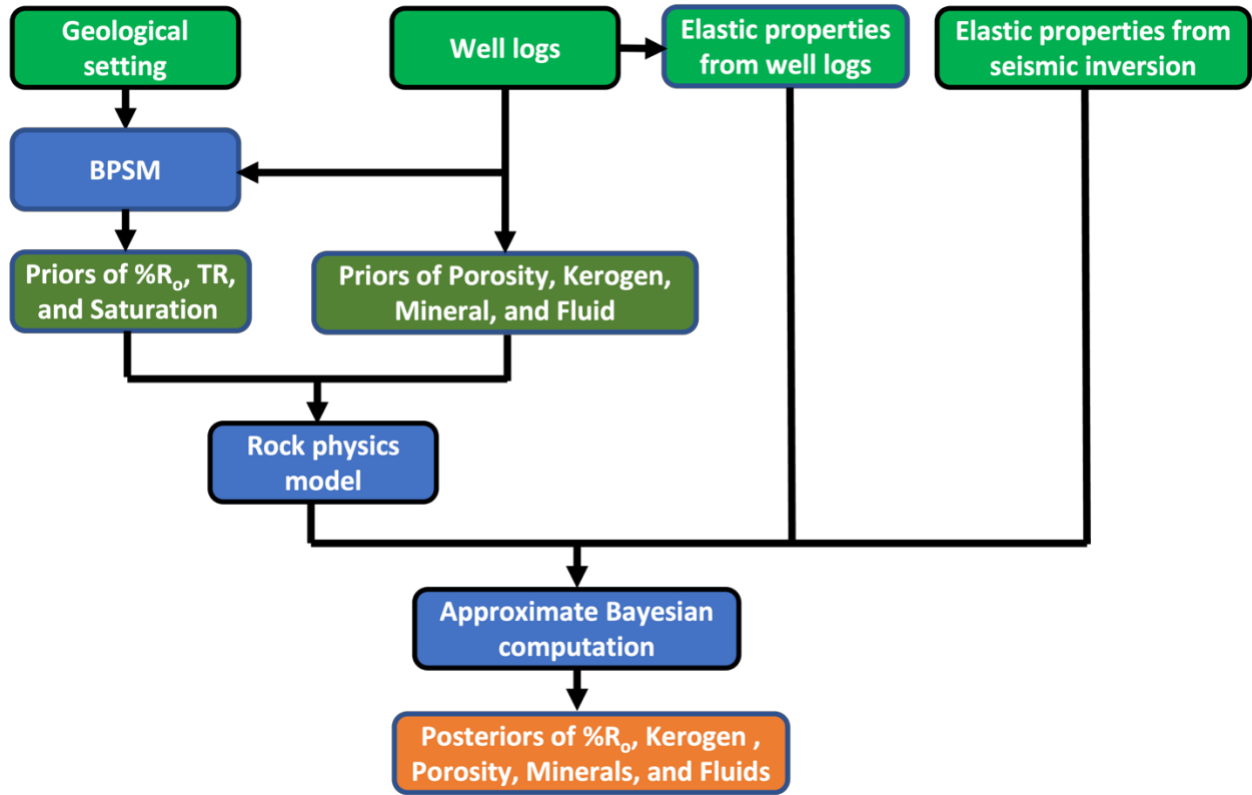


Figure 1. Proposed workflow for rock physics model inversion. BPSM, %R<sub>o</sub>, and TR refer to Basin and Petroleum System Modeling, vitrinite reflectance, and transformation ratio, respectively.

## 2.2 Thermal-maturation dependent rock physics model for organic-rich mudrocks

In this study, a thermal-maturation dependent rock physics model is applied to model unconventional shale source rock (Figure 2) (Al Ibrahim et al., 2020). The rock physics model separately considers the contributions from kerogen and inorganic matrix. For inorganic rock component, elastic moduli of mineral mixture are modeled using Voigt-Reuss-Hill average and fluid mixture are modeled using Reuss lower bound. For organic rock component, the properties of kerogen are modeled as a function of thermal maturation and kerogen types considering creation of organic pores, conversion of kerogen to hydrocarbon fluids, and densification of remaining solid kerogen. Pore systems are inserted into the kerogen and inorganic matrix using differential effective medium (DEM) theory (Berryman, 1995). Gassmann equations for fluid substitution (Gassmann, 1951) are applied to fill the pore systems with fluids like brine, oil, and gas. Finally, the overall effective elastic properties are obtained by combining porous kerogen and inorganic matrix using Backus average (Backus, 1962). The inputs for the models are: 1) kerogen content, 2) porosity, 3) mineralogical constituents, 4) fluid saturations (Bound water, free water, and oil in this study), 5) matrix aspect ratio, 6) vitrinite reflectance, and 7) kerogen type. The outputs from the model are 1) Bulk-modulus, 2) Shear-modulus, and 3) density from which we can calculate

the P-wave velocity  $V_p = \sqrt{\frac{K+4/3\mu}{\rho}}$  and S-wave velocity  $V_s = \sqrt{\frac{\mu}{\rho}}$ , where  $K$ ,  $\mu$ , and  $\rho$  are bulk and shear moduli, and bulk density of the rock.

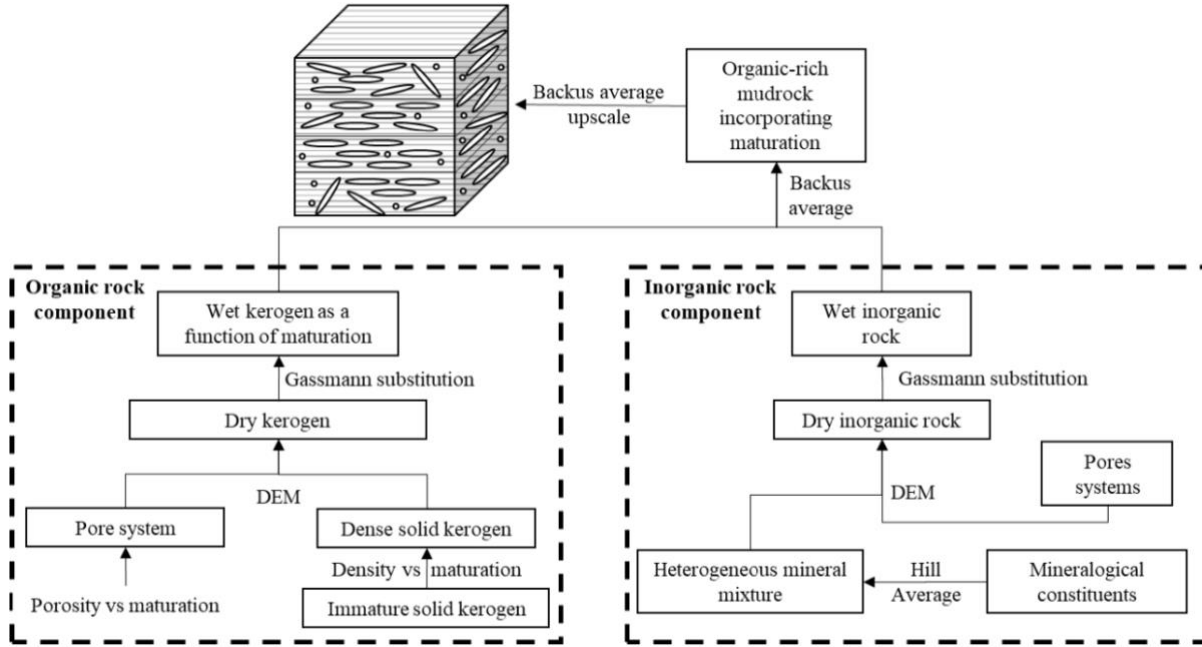


Figure 2. Workflow for constructing thermal-maturation dependent rock physics model for organic-rich mudrocks (from Al Ibrahim et al., 2020).

## 2.3 Approximate Bayesian Computation

ABC has been successfully applied in various scientific disciplines, including ecology (Beaumont, 2010), epidemiology (Minter and Retkute, 2019), and genetics (Beaumont et al., 2002), but its application to rock physics inversion remains relatively unexplored.

The rock physics model inversion can be understood in a Bayesian framework (Eq. 1).

$$p(\theta|D) = \frac{p(D|\theta)p(\theta)}{p(D)} \quad (1)$$

where  $p(\theta|D)$  is the posterior distributions of source rock properties,  $p(D|\theta)$  is the likelihood,  $p(\theta)$  is the prior distribution of source rock properties, and  $p(D)$  is the data (Elastic properties from well log or seismic signatures).

The likelihood function is of curial importance for all model-based statistical inference but might be computationally costly to evaluate for complex models (Sunnåker et al., 2013). Approximate Bayesian computation (ABC) is a likelihood free inference method first proposed by Rubin (1984). ABC can approximate the likelihood function by Monte Carlo simulations of a large number of models and their associated synthetic data, and comparing them with the observed data. More precisely, parameter values  $\theta$  are first sampled from the prior distributions. For each sampled

parameter  $\theta$ , a forward model  $M$  parameterized by  $\theta$  is run to generate a dataset  $\hat{D}$ . The generated dataset  $\hat{D}$  is accepted if a statistical distance between the generated dataset  $\hat{D}$  and the observed dataset  $D$  is smaller than a predefined tolerance  $\varepsilon$  (Eq. 2).

$$\rho(\hat{D}, D) \leq \varepsilon \quad (2)$$

where  $\rho(\cdot)$  is a distance measurement between simulated  $\hat{D}$  and observed  $D$ . If the data is high dimensional, then using summary statistics can map high dimensional data to low dimensional summaries of information which can improve computational efficiency (Eq. 3).

$$\rho(S(\hat{D}), S(D)) \leq \varepsilon \quad (3)$$

where  $S(\cdot)$  is a summary statistics.

## 2.4 Weighted Mahalanobis distance for ABC

Weighting the distance between observed and simulated data in Approximate Bayesian Computation (ABC) is crucial for accurately capturing differences within the dataset. For example, different features of the data may have varying levels of importance, requiring tailored emphasis to reflect their impact accurately. Additionally, features often vary on different scales, and without weighting, features with larger scales could disproportionately influence the distance calculation. Furthermore, if a forward model used in ABC for inversion performs well at predicting some output variables but poorly at others, this can introduce bias or inconsistency in the inference process if we weight them equally in the distance calculation. Therefore, we propose weighting the distances to account for differences in feature scales, feature importance, correlations between features, and modeling errors, ensuring more robust and reliable inference.

The concept of weighting involves combining the reciprocal of the mean squared error (MSE) between the normalized measured and modeled elastic properties from the calibration well. The reciprocal of the MSE highlights the significance of each elastic property. Consequently, variables with lower MSEs have higher weights in the distance calculation, while those with higher MSEs are assigned lower weights. The Mahalanobis distance can accounts for correlations of variables within the dataset. The weighted Mahalanobis distance  $D$  is defined in Eq. 4. More specific steps to compute distances in this work are:

1. Normalize the elastic properties in prior, modeled, measured, and target datasets:

$$y'_i = \frac{y_i - \mu_{prior}}{\sigma_{prior}}$$

Where  $y_i$  is the value of the variable ( $y$  are  $v_p$ ,  $v_s$ , density  $\rho$  in this study and  $i$  is the index of value) from the prior, modeled, measured, and target datasets.  $y'_i$  is the normalized variable.  $\mu_{prior}$  and  $\sigma_{prior}$  are the mean and the standard deviation of the variable across the prior dataset. The prior dataset is generated from the rock physics model using the prior petrophysical distributions. The modeled dataset is simulated by the rock physics model using the measured petrophysical properties from a calibration well. The measured dataset is actual elastic properties from the calibration well. The target dataset is the elastic properties from new well logs or seismic sections that we want to invert.

2. Calculate the covariance matrix  $S$  of the normalized prior dataset:

$$S = \begin{bmatrix} 1 & Cov(v_{p'prior}, v_{s'prior}) & Cov(v_{p'prior}, \rho'_{prior}) \\ Cov(v_{s'prior}, v_{p'prior}) & 1 & Cov(v_{s'prior}, \rho'_{prior}) \\ Cov(\rho'_{prior}, v_{p'prior}) & Cov(\rho'_{prior}, v_{s'prior}) & 1 \end{bmatrix}$$

Where  $Cov(a, b)$  represents the correlation coefficient between variables  $a$  and  $b$ .

3. Calculate the weight matrix:

$$W = \begin{bmatrix} w_{v_p} & 0 & 0 \\ 0 & w_{v_s} & 0 \\ 0 & 0 & w_{\rho} \end{bmatrix}$$

Where  $w = \frac{1}{MSE(y'_{modeled}, y'_{measured})}$ ,  $y'_{modeled}$  is normalized modeled elastic properties using rock physics model and petrophysical properties from the calibration well,  $y'_{measured}$  is normalized measured elastic properties from the calibration well, and  $MSE(y'_{modeled}, y'_{measured})$  is the mean-squared error between the normalized modeled and measured elastic properties.

4. Calculate the weighted Mahalanobis distance between all the elastic properties in the normalized prior dataset and a single normalized target elastic property.

$$D = \sqrt{(y'_{prior} - y'_{target})^T W S^{-1} W (y'_{prior} - y'_{target})} \quad (4)$$

Where  $y' = \begin{bmatrix} v'_p \\ v'_s \\ \rho' \end{bmatrix}$ ,  $W$  is the weight matrix, and  $S$  is the covariance matrix.

5. Set a threshold to accept the weighted Mahalanobis distances. The threshold can be a tolerance level or based on a specified number of accepted prior samples. In this work, we accept the nearest  $N$  samples to the target elastic property.

6. Calculate the probability distributions of the petrophysical properties associated with the accepted samples using kernel density estimation (KDE). These distributions represent the posterior probabilities of the petrophysical properties.

7. Repeat steps 4 to 6 to obtain the posterior distributions of petrophysical properties along the entire target well log or seismic section.

### 3. Monte Carlo sensitivity analysis of the rock physics model

#### 3.1 Monte Carlo simulation of trends with different ranges of inputs

The constructed rock physics model is high-dimensional and non-linear. The inputs of the rock physics model are listed in Table 1. Elastic properties of minerals like quartz, Calcite, Dolomite, and Pyrite are relatively well known. However, elastic properties of clay minerals like illite and chlorite have wide range of values in literature, the difference being related to different experimental techniques as well as fine-grained nature and bound fluids of clay minerals (Mondol et al., 2008). Elastic properties of kerogen are not well constrained (Vernik and Landis, 1996; Mavko et al., 2020) Therefore, in this study, elastic properties of kerogen and clay minerals are considered as uncertain rock physics model parameters. These properties are set in reasonable prior ranges and later can be refined by rock physics model calibration using well logs.

To investigate the variations of output elastic properties, we randomly sample the input variables within different ranges. The mineral and fluid properties and the variable distributions used in Monte Carlo sampling are listed in Table 1 and Table 2, respectively. The Dirichlet distribution is used for volumetric quantities to ensure that they sum up to one. There are several observations in the cross plots for different types of kerogens (Figure 3): 1) Higher volumetric percentages of porosity and kerogen will lower P-wave impedance. 2) For all three types of kerogens, varying volumetric percentages of porosity and kerogen has limited impacts on  $V_P/V_S$ .

Component	K [GPa]	G [GPa]	$\rho$ [g/cc]	Reference
Kerogen	(2, 10)	(2, 5)	$f(R_0)$	(Vernik and Landis, 1996; Mavko et al., 2020)
Quartz	37	44	2.65	(Carmichael, 2017)
Calcite	76.8	32	2.71	(Simmons, 1965)
Illite	(20, 60)	(5, 30)	(2.7, 2.9)	(Mondal et al., 2008; Wang et al., 2001)
Chlorite	(20, 60)	(5, 30)	(2.7, 3.0)	(Mondal et al., 2008; Wang et al., 2001)
Dolomite	94.9	45	2.87	(Humbert, 1972)
Pyrite	139	112.3	5.01	(Whitaker et al., 2010)
Bound water	2.2	0	1.0	(Mavko et al., 2020)
Free water	2.2	0	1.0	(Mavko et al., 2020)
Oil	1.02	0	0.8	(Batzle & Wang, 1992)

Table 1. Mineral properties used in rock physics modeling. Properties of kerogen, illite, and chlorite have uniform distributions. Deterministic values can be obtained by Monte Carlo rock physics model calibration using well logs. Kerogen density is a function of vitrinite reflectance  $R_0$ .

Input variable	Distribution	Range
Kerogen type	Categorical	(I, II, III)
Vitrinite reflectance	Uniform	(0.23, 1.6)
Kerogen	Uniform	(0, 0.2)
Porosity	Uniform	(0, 0.2)
Matrix aspect ratio	Uniform	(0.001, 0.2)
Quartz	Dirichlet	(0, 1)
Calcite	Dirichlet	(0, 1)
Illite	Dirichlet	(0, 1)
Chlorite	Dirichlet	(0, 1)



Dolomite	Dirichlet	(0, 1)
Pyrite	Dirichlet	(0, 1)
Bound water	Dirichlet	(0, 1)
Free water	Dirichlet	(0, 1)
Oil	Dirichlet	(0, 1)

Table 2. Input variable distributions used in Monte Carlo sampling for elastic property trends analysis and Monte Carlo sensitivity analysis. Kerogen, porosity, minerals, and fluids are volumetric.

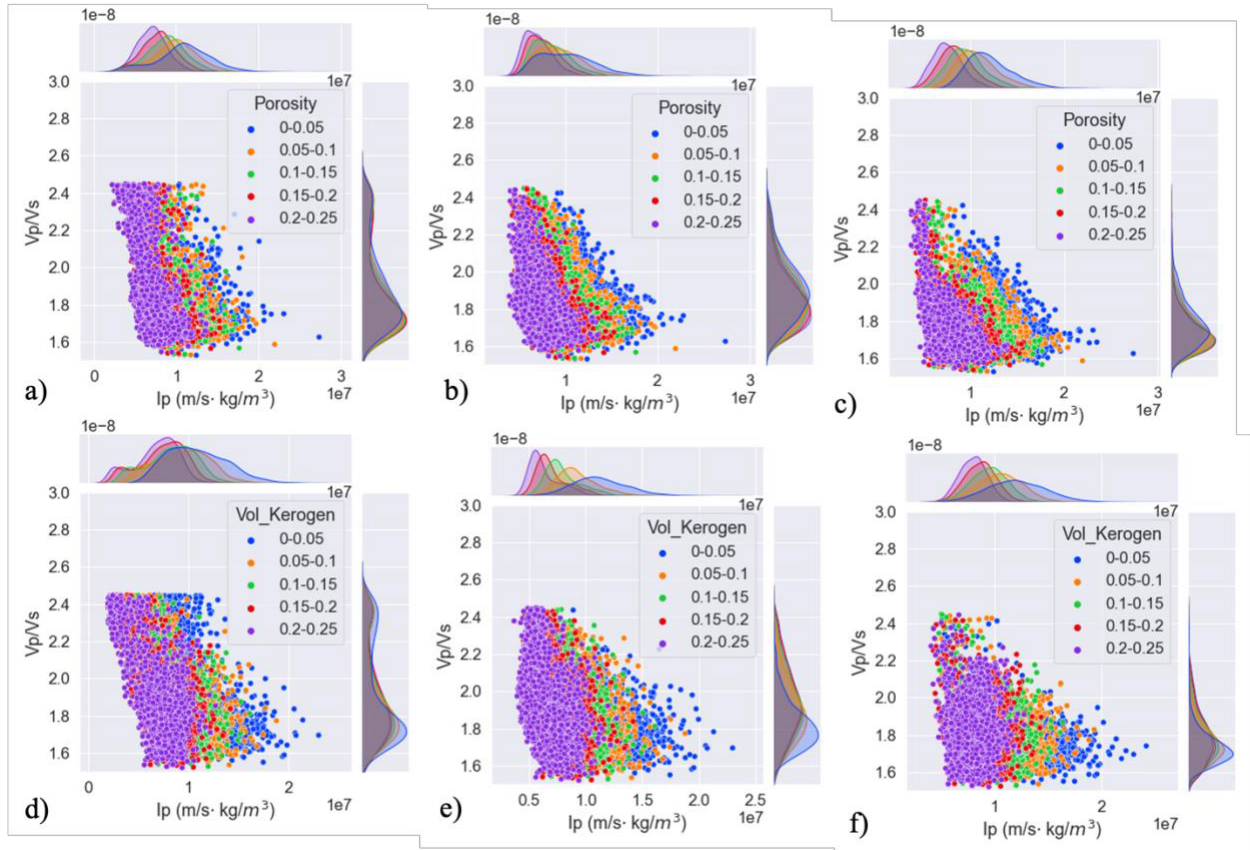


Figure 3. Crossplots of elastic properties ( $V_p/V_s$  and P-wave impedance) for Type I, Type II, and Type III kerogen, showing different ranges of porosity and volumetric kerogen content. Each range includes 2,000 realizations. (a), (b), and (c) illustrate the elastic properties trends by varying porosity for Type I, Type II, and Type III kerogen, respectively. (d), (e), and (f) depict the elastic properties trends by varying volumetric kerogen content for Type I, Type II, and Type III kerogen, respectively.

### 3.2 Sensitivity analysis

Distance-based generalized sensitivity analysis (DGSA) (Fenwick et al., 2014; Park et al., 2016) is applied to analyze the sensitivity of the output elastic properties to the rock physics model input

variables. The steps to implement DGSA are: 1). Randomly generate input variables and run the forward simulator (rock physics model) to get the response variables (elastic properties). 2). Classify and group the response variables into predefined number of clusters using k-medoids clustering. 3). Calculate the cumulative distribution function (CDF) of the input variables for each cluster and the distance between the prior CDF of all the samples and conditional CDF of each cluster using the L1 norm. 4). Test whether the distance is statistically significant using bootstrap resampling. 5). The CDF distance is standardized using the bootstrap results and is defined as a sensitivity measure for each variable. The input variables include porosity, kerogen, mineral fractions, fluid fractions, matrix aspect ratio, and vitrinite reflectance. The response variables are  $I_p$  and  $I_s$  (P-wave and S-wave impedance). The variable distributions used in Monte Carlo sampling are listed in Table 1 and Table 2. The sensitivity analysis result in Figure 4 shows that the top 5 sensitive input variables are porosity, volume fraction of kerogen, kerogen type, vitrinite reflectance, and matrix aspect ratio.

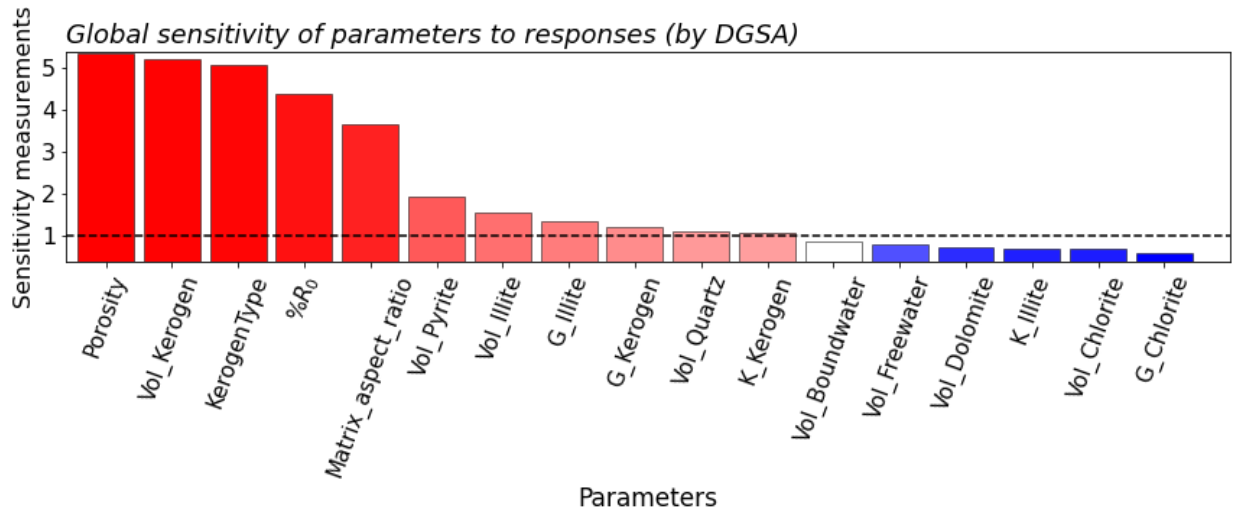


Figure 4. Sensitivity analysis of the rock physics model output elastic properties ( $I_p$  and  $I_s$ ) to the inputs using DGSA. The top 5 sensitive input variables are porosity, volume fraction of kerogen, kerogen type, vitrinite reflectance, and matrix aspect ratio.

#### 4. Synthetic example of rock physics inversion using ABC

A synthetic case is experimented to test the feasibility of rock physics inversion workflow using ABC. Uncertain properties of kerogen, illite and chlorite are randomly sampled and fixed for the following Monte Carlo simulations. A set of input variables are randomly sampled from Table 2 and the kerogen type is set as type III. This set of input variables represent the observed values in Figure 5. Then sets of elastic properties ( $I_p, I_s$ ) and ( $V_p, V_s, \rho$ ) are calculated using the constructed rock physics model. These sets of elastic properties ( $I_p, I_s$ ) and ( $V_p, V_s, \rho$ ) are used for inversion. When applying ABC for inverting the elastic properties, we compare the results when inverting elastic properties ( $I_p, I_s$ ) versus inverting ( $V_p, V_s, \rho$ ). We also compare the results when using Euclidean distance versus Mahalanobis distance as acceptance criteria. The ABC steps are as follow: 1) Randomly generate a test set (100,000) of input variables from Table 2 and calculate the corresponding sets of elastic properties ( $I_p, I_s$ ) and ( $V_p, V_s, \rho$ ) by the rock physics model. 2)

Calculate Euclidean distances and Mahalanobis distance between the sampled 100,000 sets of elastic properties ( $I_p, I_s$ ) and ( $V_p, V_s, \rho$ ) and the set for inverting (i.e., corresponding to the observed value). 3). Find the 1,000 samples that are nearest to the elastic properties that are being used for the inversion. 4). Calculate Probability density functions (PDF) of the input variables of the 1,000 nearest samples using kernel density estimation. The obtained PDFs are the posteriors of input variables. An example of inverting observed elastic properties ( $I_p, I_s$ ) and ( $V_p, V_s, \rho$ ) using ABC is shown in Figure 5. A comparison of prior ( $I_p, I_s$ ), accepted ( $I_p, I_s$ ), and observed ( $I_p, I_s$ ) when using Euclidean distance and Mahalanobis distance as acceptance criteria is in Figure 6. There are some observations in the inversion results: 1) For sensitive variables like porosity and kerogen, there are more updates in their posteriors compared to insensitive variables like free water and bound water. 2) Posteriors obtained by inverting ( $V_p, V_s, \rho$ ) have less uncertainty than inverting ( $I_p, I_s$ ). 3) In Figure 6, accepted ( $I_p, I_s$ ) samples scatter around the observed ( $I_p, I_s$ ) when using Euclidean distance while accepted ( $I_p, I_s$ ) samples using Mahalanobis distance have strong correlation that is similar the prior correlation. 4) Overall, the posteriors obtained by inverting ( $V_p, V_s, \rho$ ) and incorporating the Mahalanobis distance yield the most accurate results.

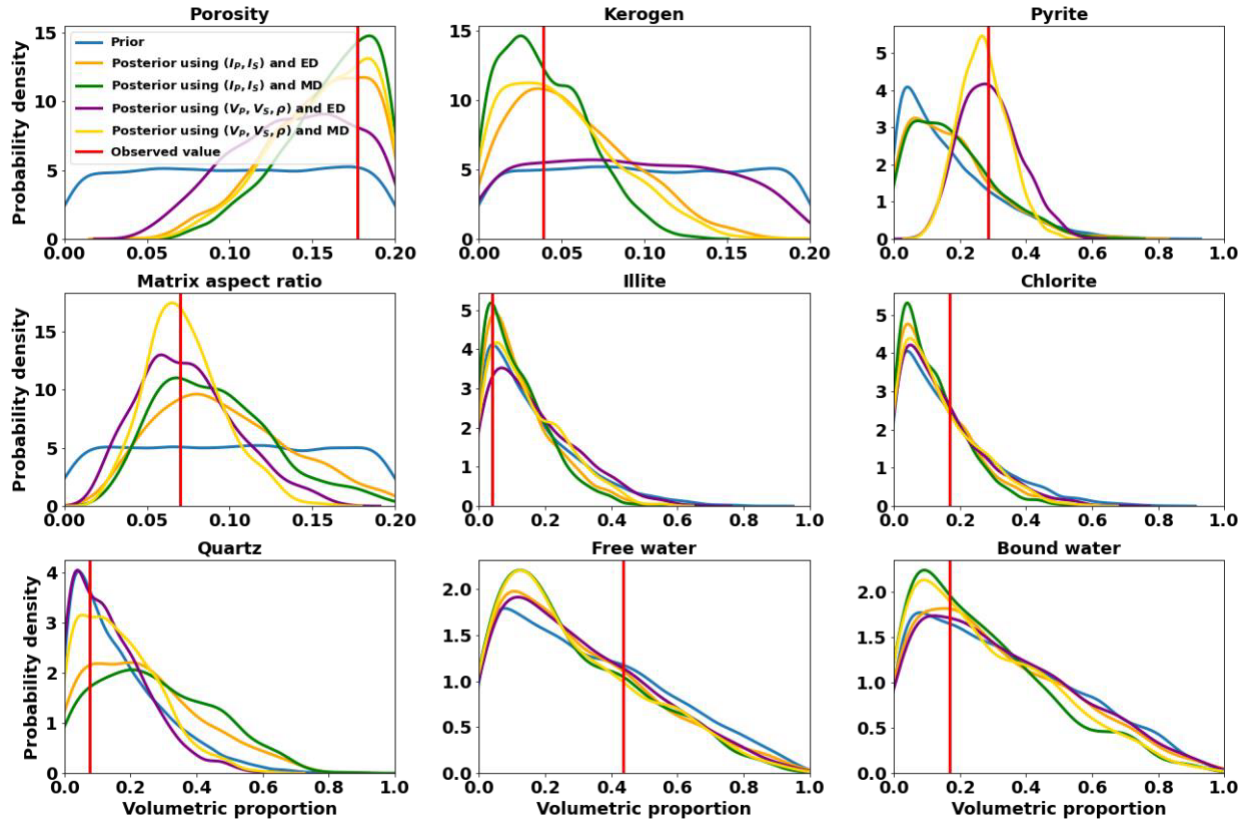


Figure 5. An example of inversion results using ABC. The blue curves are prior, the orange curves are posteriors when inverting the observed ( $I_p, I_s$ ) using Euclidean distance, the green curves are posteriors when inverting the observed ( $I_p, I_s$ ) using Mahalanobis distance, the purple curves are posteriors when inverting the observed ( $V_p, V_s, \rho$ ) using Euclidean distance, the yellow curves are posteriors when inverting the observed ( $V_p, V_s, \rho$ ) using Mahalanobis distance, and the red vertical lines are the corresponding observed values.  $I_p$  is P-wave impedance,  $I_s$  is S-wave

impedance,  $V_P$  is P-wave velocity,  $V_S$  is S-wave velocity,  $\rho$  is density. ED and MD refer to Euclidean distance and Mahalanobis distance, respectively.

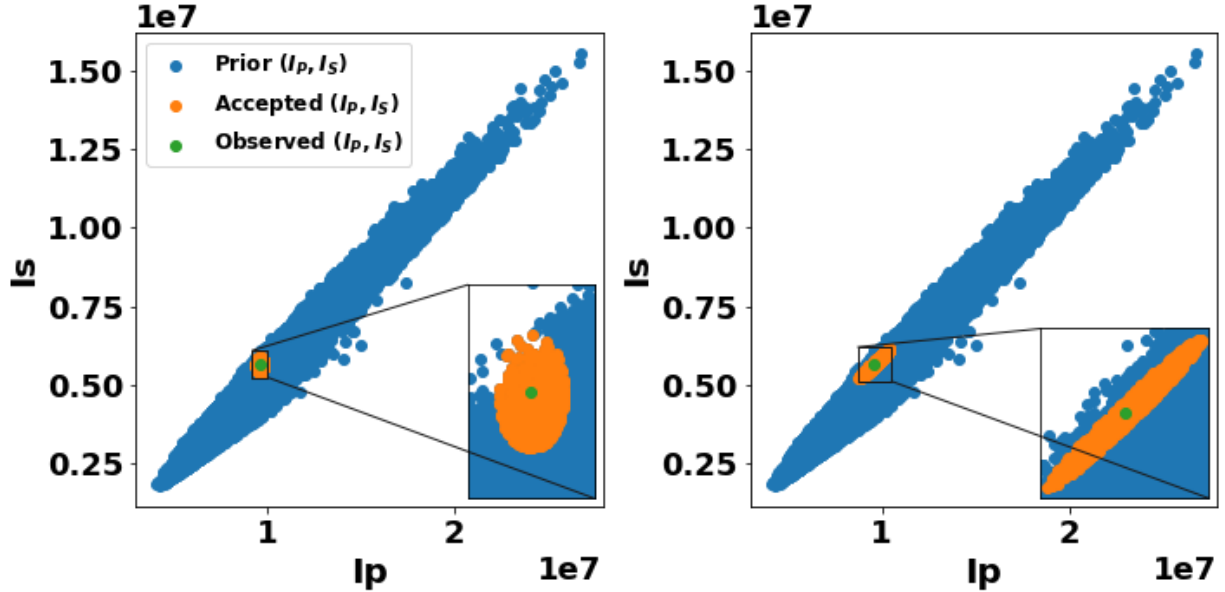


Figure 6. Scatter plots of prior, accepted, and observed ( $I_P, I_S$ ) using Euclidean distance and Mahalanobis distance. The blues dots are prior ( $I_P, I_S$ ), the orange dots are accepted ( $I_P, I_S$ ), and the green dots are the observed ( $I_P, I_S$ ) for inverting.

## 5. Field example: Source rock potentials of Unconventional shale in the Canning Basin, Australia

We apply the above workflow to a field data set from the Canning Basin, Australia. The Canning Basin is the largest sedimentary basin in Western Australia that has increasing unconventional resource potential (Alshakhs and Rezaee, 2019). The Goldwyer Formation of the Canning Basin has significant shale gas and oil potentials in the basin (EIA, 2015). The Goldwyer formation can be divided into three zones based on source rock lithofacies: upper shale (Goldwyer I), middle carbonates (Goldwyer II), and lower shale (Goldwyer III) (Foster et al., 1986). The Goldwyer III has been proven to have unconventional hydrocarbon potential (van Hattum et al., 2019). This field example focuses on the Goldwyer III Formation.

### 5.1 Data introduction

The study area includes two wells, Cyrene-1 and Theia-1, both of which penetrate the Goldwyer formation (Figure 7). These wells provide geochemical, petrophysical, and sonic logs (Figure 8 and 9). Additionally, a 2D pre-stack seismic inversion section across the Theia-1 well is available, containing P-wave impedance, density, and  $V_P/V_S$  which are then converted to  $V_P$ ,  $V_S$ , and  $\rho$  for rock physics inversion. A portion of the pre-stack seismic inversion section near the Theia-1 well is used in the subsequent rock physics inversion (Figure 9). Vitrinite reflectance from a 3D basin model is available in the study area and will be used to calibrate the rock physics model and inversion (Finder Exploration, 2016) (Figure 10).





Figure 7. Locations of wells and seismic survey in the Canning Basin. Red dots indicate well locations, with an approximate spacing of 116 km, while the blue curve represents the seismic survey.

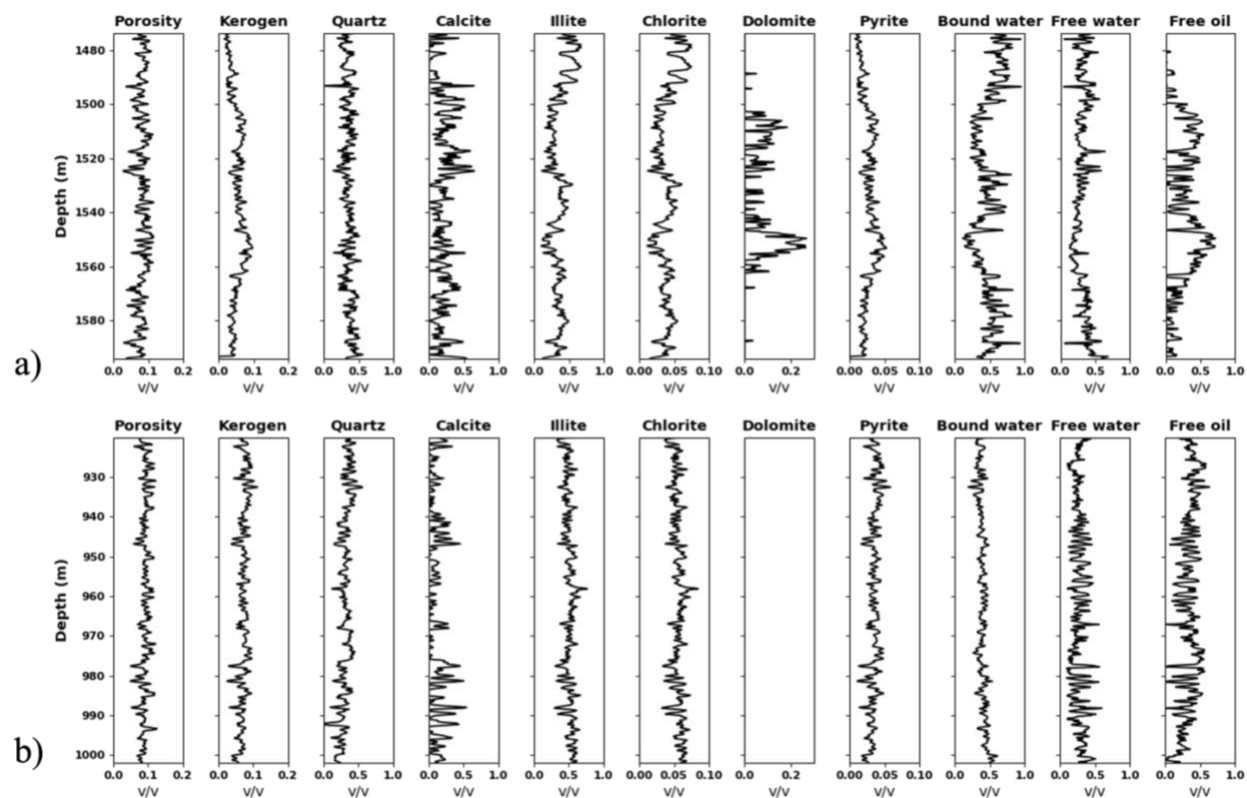


Figure 8. Well-log data, including porosity, kerogen, minerals, and fluids. The minerals form the matrix and are normalized to sum to 1. Fluid saturations, assumed to fill the pore system, are also normalized to sum to 1. The sum of porosity, kerogen, and matrix equals 1. (a) Theia-1 well. (b) Cyrene-1 well, where no dolomite is present.

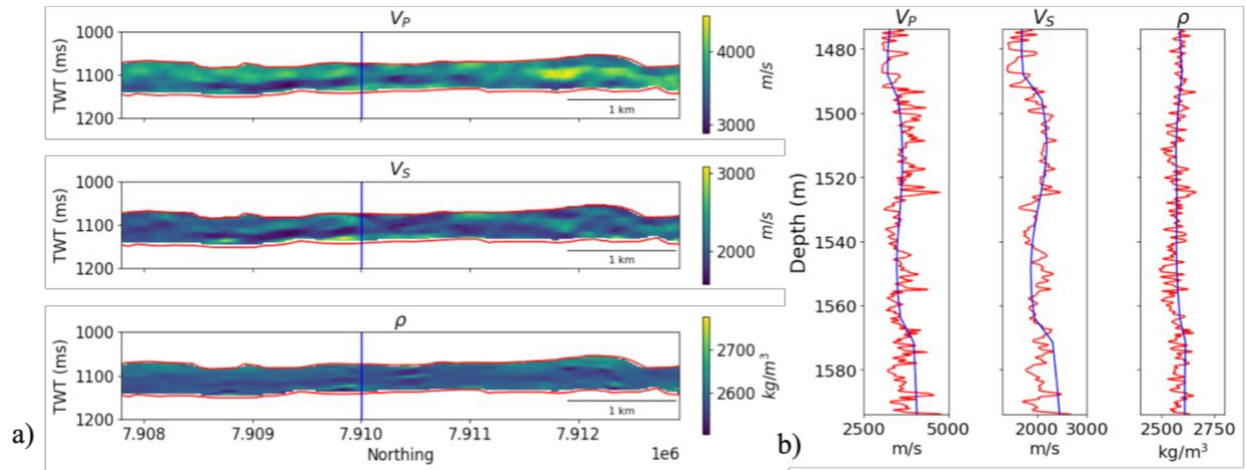


Figure 9. a) A portion of the pre-stack seismic inversion section near the Theia-1 well. The blue vertical line is the Theia-1 well, the red curves are the top and the bottom of the Goldwyer III Formation. b) Comparisons of  $V_p$ ,  $V_s$ ,  $\rho$  from well log and seismic inversion in the Goldwyer III Formation in the Theia-1 well. The red curves are from well log, the blue curves are from seismic inversion.

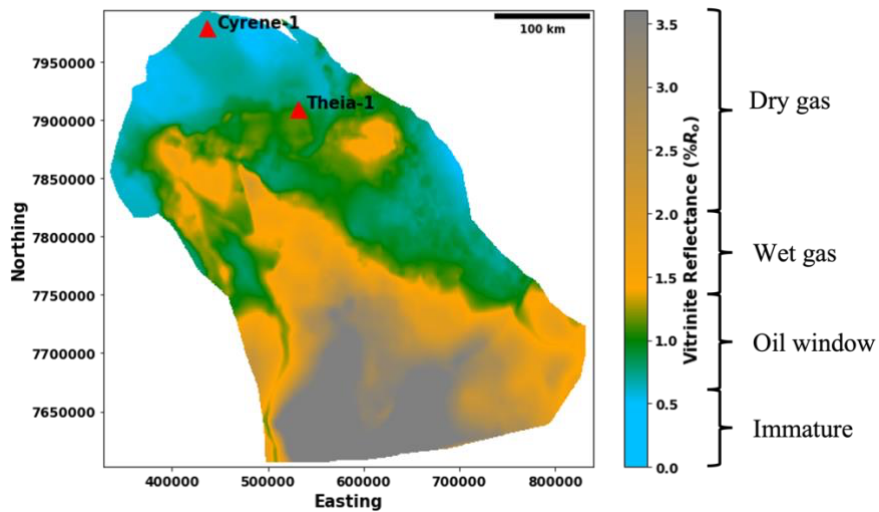


Figure 10. Vitrinite Reflectance ( $\%R_o$ ) modeling at 0 Ma in the Canning Basin and hydrocarbon generation windows (Finder Exploration, 2016; Egbobawaye, 2017). The red triangles indicate the well location. The  $\%R_o$  of Cyrene-1 and Theia-1 are 0.63 and 1.04 separately.

### 5.1 Monte Carlo rock physics model calibration by well logs

In Table 1, properties of clay minerals are uncertain. Therefore, Theia-1 well is used for calibrating the uncertain properties of clay minerals before applying the model to rock physics inversion. It is important to mention that matrix aspect ratio is a sensitive parameter in the rock physics model but is not available in the well log. Varying the aspect ratio at each depth can address the complex pore system and improve the accuracy of the rock physics model (Guo et al., 2021). Therefore, instead of fixing the matrix aspect ratio for the whole well, we vary the matrix aspect ratio at each

depth when calibrating the moduli of clay minerals and kerogen. In the inversion process, the matrix aspect ratio is one of the inverted properties.

For mineral density calibration, mineral volume fractions from geochemical log are input to the rock physics model. A grid search method with interval of 0.01 g/cc is applied to minimize the MSE between the modelled density and the measured density log. The accepted illite density is 2.84 g/cc and chlorite density is 2.71 g/cc. Then, the accepted densities are validated by Cyrene-1 (Figure 11).

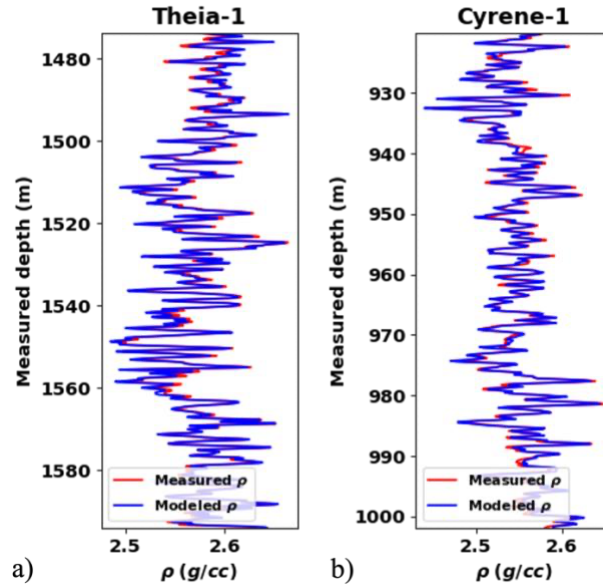


Figure 11. Comparisons of the measured density logs and the modeled density logs with minimum MSE. a) Theia-1 well. b) Cyrene-1 well. The blue curves are modeled density logs and the red curves are measured density logs.

For mineral and kerogen moduli calibration, a Monte Carlo rock physics model calibration approach is applied to find optimal moduli of kerogen, illite, and chlorite. Bulk and shear modulus of kerogen, illite, and chlorite are assumed to be uniformly distributed and the ranges are specified in Table 1.

The steps of the moduli calibrations are:

1) Bulk modulus  $K$  and shear modulus  $G$  of kerogen, illite, and chlorite are randomly sampled from Table 1.

2) Poisson's ratio  $\nu$  is calculated by  $\nu = \frac{3K-2G}{2(3K+G)}$ . If  $\nu$  of clay minerals is in the range of (0.1, 0.4) (Wang et al., 2001; Mondal et al., 2008; Hedan et al., 2015) and  $\nu$  of kerogen is in the range of (0.2, 0.35) (Kashinath et al., 2019; Wu and Firoozabadi, 2020), the sampled bulk and shear modulus are kept for next step. Otherwise, step 1 will be repeated until the Poisson's ratio is in the reasonable range.

3) For each depth in Theia-1 well, volume fractions of minerals, kerogen, and fluids, vitrinite reflectance, porosity from well logs are input to the rock physics model. Matrix aspect ratio is a

model parameter that cannot be obtained from well log. Therefore, a grid search method is applied to find optimal matrix aspect ratio of each depth that can minimize the MSE between the measured  $(V_p, V_s)$  and the modeled  $(V_p, V_s)$  at each depth.

4) After finding the optimal matrix aspect ratio of each depth, the MSE between the measured  $(V_p, V_s)$  and the modeled  $(V_p, V_s)$  of the whole well is calculated.

5) Steps 1-4 are repeated N times, and the bulk modulus K and shear modulus G of kerogen, illite, and chlorite that have minimum MSE between the measured  $(V_p, V_s)$  and the modeled  $(V_p, V_s)$  of the whole well are finally accepted.

6). The calibrated rock physics model is validated using the Cyrene-1 well. The same grid search method in step 3 is applied here to optimize the matrix aspect ratio at each depth that can minimize the MSE between the measured  $(V_p, V_s)$  and the modeled  $(V_p, V_s)$  at each depth.

In this case, 10,000 sets of properties are randomly generated. The accepted properties of kerogen and clay minerals with minimum MSE are list in Table 3. The cross-plots of measured and modeled  $(V_p, V_s, \rho)$  of Theia-1 and Cyrene-1 after calibration are shown in Figure 12.

Component	K [GPa]	G [GPa]	$\rho$ [g/cc]
Kerogen	9.2	3.6	$f(R_0)$
Illite	28.2	6.1	2.84
Chlorite	39.2	8.8	2.71

Table 3. Accepted properties of kerogen and clay minerals from Monte Carlo rock physics model calibration. K is bulk modulus, G is shear modulus, and  $\rho$  is density.  $R_0$  is vitrinite reflectance. Density of kerogen is a function of vitrinite reflectance.



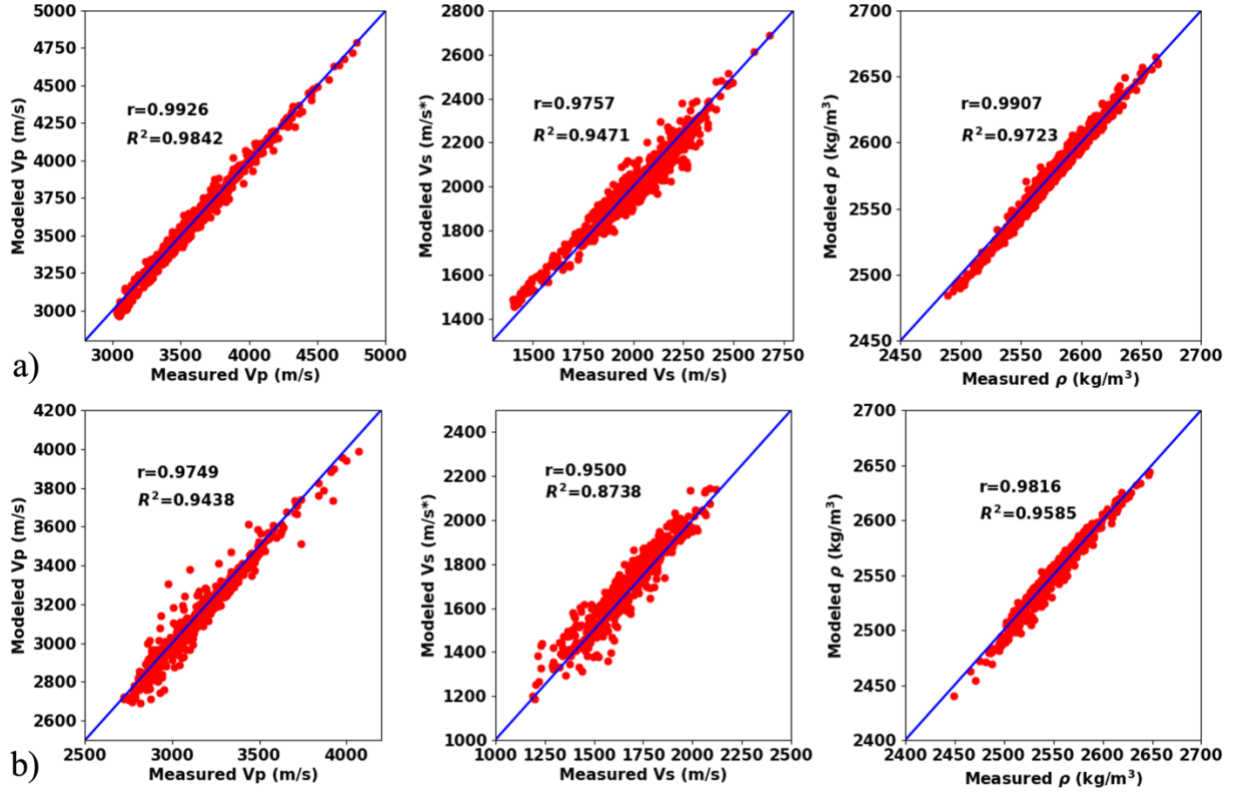


Figure 12. Crossplots of measured and modeled ( $V_p$ ,  $V_s$ ,  $\rho$ ) of Theia-1 well. a) Theia-1 well. b) Cyrene-1 well.  $V_p$  is compressional velocity,  $V_s$  is shear velocity,  $\rho$  is density,  $r$  is the Pearson correlation coefficient, and  $R^2$  is the coefficient of determination.

Prior falsification is performed to ensure consistency between modeled and real data (Scheidt et al., 2018). The new priors are estimated from the Theia-1 well and are shown in Table 4. Impedances ( $I_p$ ,  $I_s$ ) are modeled using the prior and calibrated rock physics model, then are compared with real impedance data from sonic log in Figure 13. The real data are in the range of the priors which means the rock physics model cannot be falsified.

Input variable	Distribution	Range
Kerogen type	Categorical	III (Iqbal et al., 2022)
Vitrinite reflectance	Uniform	(0.23, 1.6)
Kerogen	Uniform	(0, 0.15)
Porosity	Uniform	(0, 0.15)
Matrix aspect ratio	Uniform	(0.001, 0.2)
Quartz	Dirichlet	(0, 0.6)
Calcite	Dirichlet	(0, 0.8)
Illite	Dirichlet	(0, 0.8)
Chlorite	Dirichlet	(0, 0.1)
Dolomite	Dirichlet	(0, 0.1)
Pyrite	Dirichlet	(0, 0.06)
Bound water	Dirichlet	(0, 1)
Free water	Dirichlet	(0, 1)

Oil	Dirichlet	(0, 1)
-----	-----------	--------

Table 4. Prior distributions of input variables.

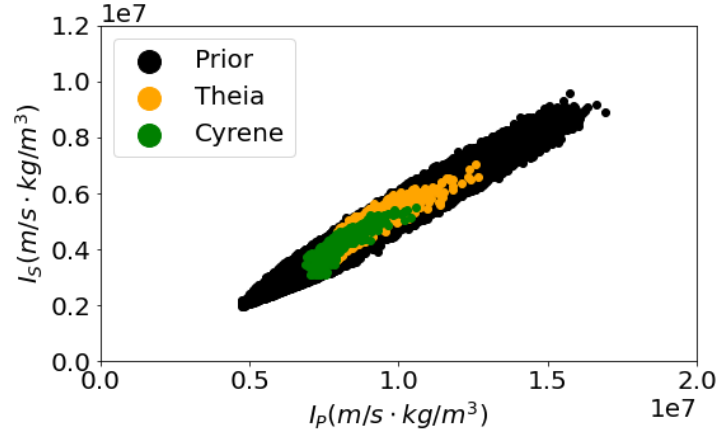


Figure 13. Consistency check between modeled impedances and real impedances from well logs.

## 5.2 Outlier detection for seismic inversion

Outliers in seismic inversion can result from various factors such as noise and errors in data acquisition, geological anomalies, processing artifacts, and limitations of the inversion algorithm. Removing these outliers is essential to improve the accuracy and reliability of the rock physics inversion. Here, we detect and remove the outliers in the seismic inversion using the robust Mahalanobis distance (RMD). The Minimum Covariance Determinant (MCD) estimator (Rousseeuw, 1984) is used to estimate the covariance matrix of the seismic inversion. The RMD of each point in the seismic inversion is then calculated, and a threshold of  $\pm 3$  standard deviations is set to identify and remove the outliers (Figure 14). The corresponding  $V_P$ ,  $V_S$ , and  $\rho$  sections after outlier removal are shown in Figure 15. Most of the removed outliers are located near the bottom of the Goldwyer III formation, potentially caused by formation interpretation errors or changes in lithology. The  $V_P$ ,  $V_S$ , and  $\rho$  2D sections will be used for rock physics inversion.

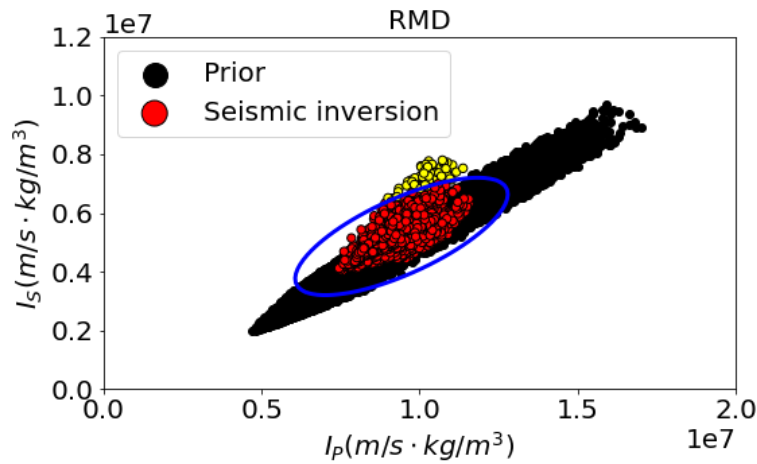


Figure 14. Seismic outlier detection using robust Mahalanobis distance with threshold of  $\pm 3$  standard deviations. The yellow points are considered as outliers.

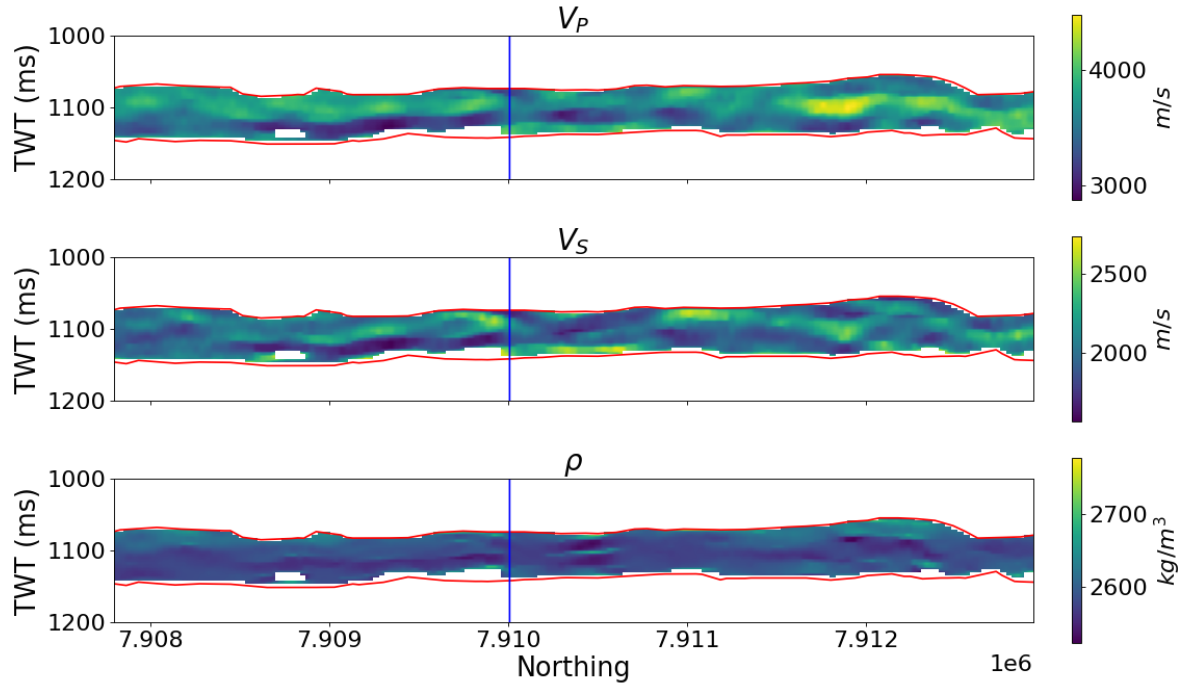


Figure 15.  $V_p$ ,  $V_s$ , and  $\rho$  sections after outlier removal. The blue line is Theia-1 well. The red curves are the top and bottom of the Goldwyer III formation.

### 5.3 Sensitivity analysis of the calibrated model using the new priors

In Section 3.2, we investigated the sensitivity of the uncalibrated rock physics model using large priors. In the field study, the rock physics model is calibrated, and the new priors are estimated from well logs. Therefore, we need to analyze the sensitivity of the calibrated rock physics model again using the new priors in Table 4. The sensitivity analysis results are shown in Figure 16. The top four sensitive variables are porosity, matrix aspect ratio, volume fraction of illite, and volume fraction of kerogen. These results suggest that fixing the matrix aspect ratio in the well logs can potentially lead to inaccurate inversion results for other properties.

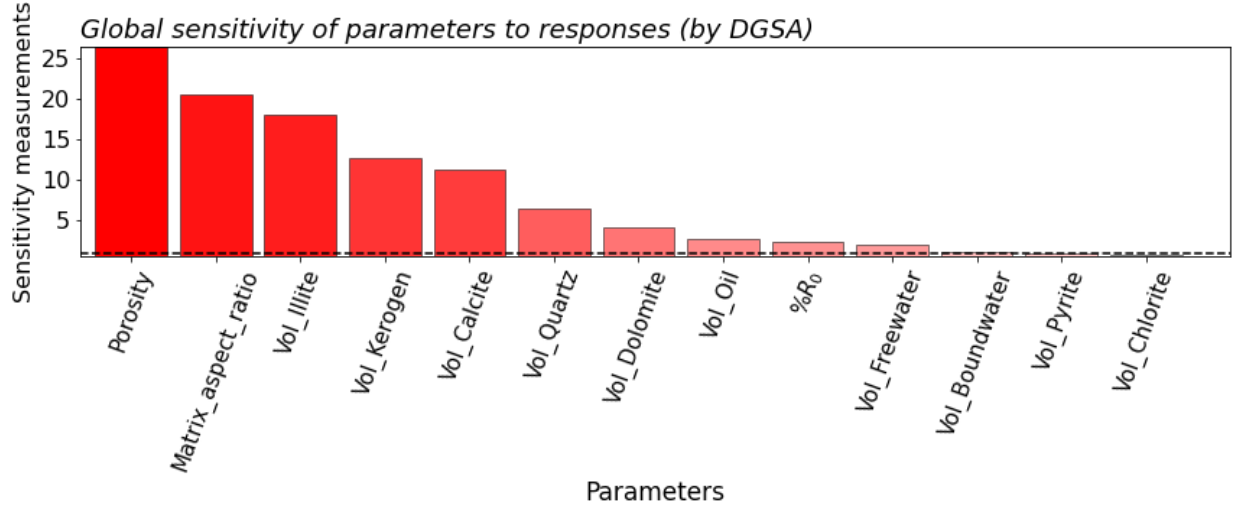


Figure 16. Sensitivity analysis of the calibrated rock physics model inputs to elastic properties ( $V_p$ ,  $V_s$ , and  $\rho$ ) using the new prior table. The top 4 input variables are porosity, matrix aspect ratio, illite, and kerogen.

#### 5.4 Weight calculations for ABC distance using the calibration well

The sensitivity analysis results indicate that the matrix aspect ratio is the second most sensitive parameter in the rock physics model. As a model parameter, the matrix aspect ratio cannot be directly obtained from well logs. It has a significant impact on velocity modeling but does not influence density modeling. Therefore, it is necessary to account for this modeling error when determining weights.

In the calibration well, all input variables except for the matrix aspect ratio are provided to the calibrated rock physics model. To account for the effect of the matrix aspect ratio at each depth, 1,000 realizations of the matrix aspect ratio are randomly sampled from the prior distributions and then input into the rock physics model. The modeled 1,000 realizations of  $V_p$ ,  $V_s$ , and  $\rho$  are averaged at each depth. This process is repeated at each depth in the whole well log. Crossplots of the average modeled and measured  $V_p$ ,  $V_s$ , and  $\rho$  in the whole well log are plot in Figure 17. Comparing the results in Figures 12 and 17, it is evident that the matrix aspect ratio significantly impacts the modeling of elastic properties. The weight matrix  $W$  and covariance matrix  $S$  for  $V_p$ ,  $V_s$ , and  $\rho$  are calculated and are listed below.

$$W = \begin{bmatrix} 16.97 & 0 & 0 \\ 0 & 7.47 & 0 \\ 0 & 0 & 405.26 \end{bmatrix}$$

$$S = \begin{bmatrix} 1 & 0.97 & 0.53 \\ 0.97 & 1 & 0.42 \\ 0.53 & 0.42 & 1 \end{bmatrix}$$

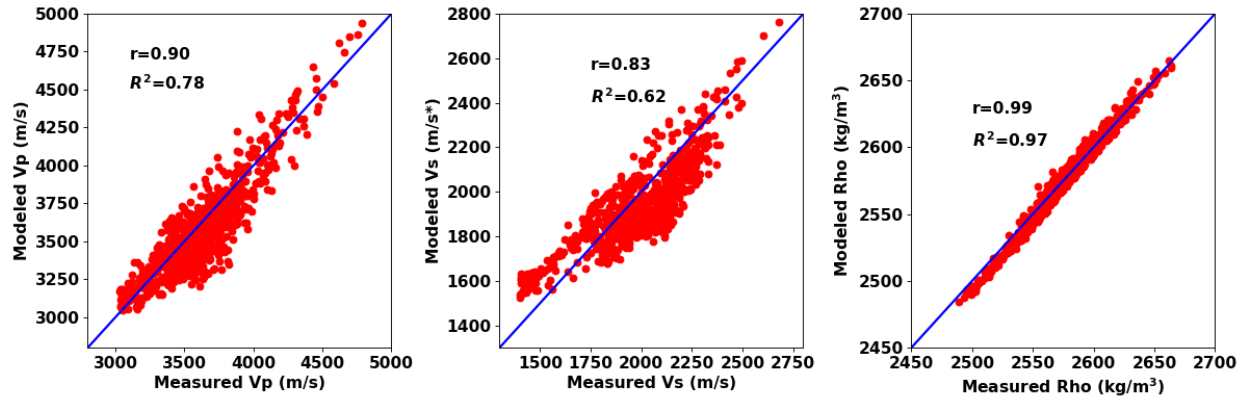


Figure 17. Crossplots of measured and average modeled ( $V_P$ ,  $V_S$ ,  $\rho$ ) of Theia-1 well when varying matrix aspect ratio.  $V_P$  is compressional velocity,  $V_S$  is shear velocity,  $\rho$  is density,  $r$  is the Pearson correlation coefficient, and  $R^2$  is the coefficient of determination.

### 5.5 Rock physics model inversion using well logs

The workflow of ABC is then applied to invert the source rock properties from well log ( $V_P$ ,  $V_S$ ,  $\rho$ ). The rock physics inversion is performed depth by depth in the well logs (Figure 18). 100,000 sets of prior ( $V_P$ ,  $V_S$ ,  $\rho$ ) are generated. At each depth, the weighted Mahalanobis distances between 100,000 sets of prior ( $V_P$ ,  $V_S$ ,  $\rho$ ) and the well log ( $V_P$ ,  $V_S$ ,  $\rho$ ) are calculated. Based on the weighted Mahalanobis distances, only the top 1% ( $V_P$ ,  $V_S$ ,  $\rho$ ) that are nearest to the well log ( $V_P$ ,  $V_S$ ,  $\rho$ ) are accepted. The distributions of the accepted prior input variables are considered as the posteriors of source rock properties at this depth. The rock physics inversion is performed at each depth independently and therefore can be run in parallel to accelerate the inversion process.

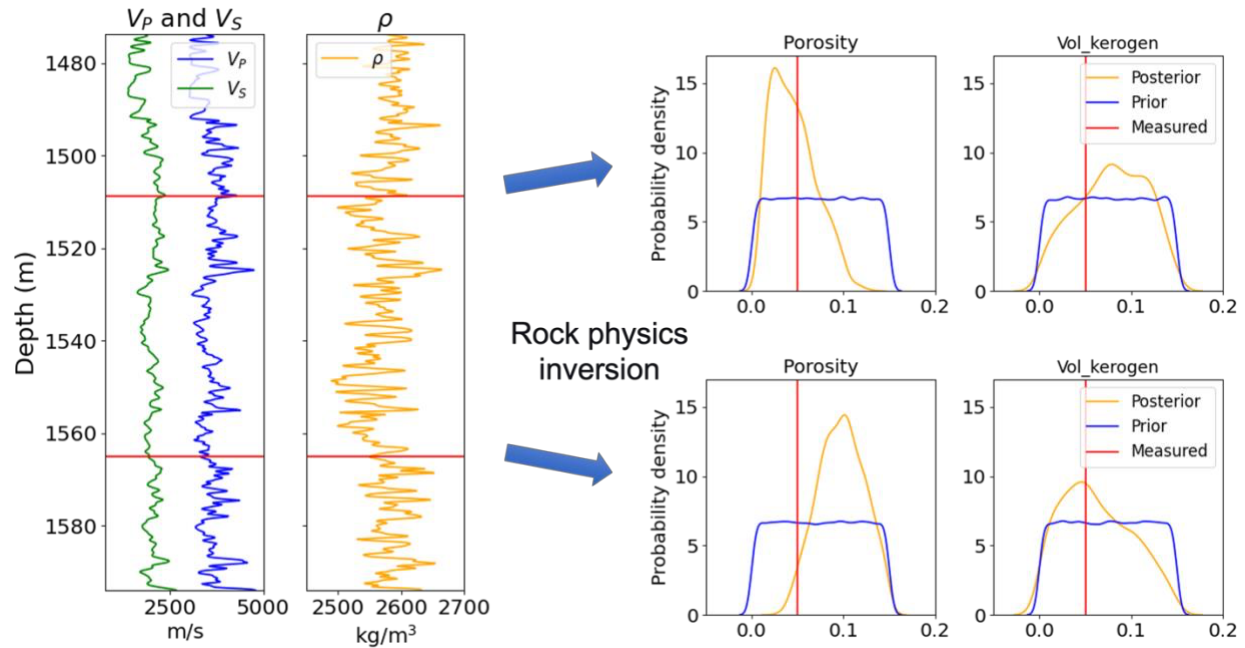


Figure 18. Illustration of rock physics inversion using ABC applied to well log. The blue arrows represent rock physics inversion with ( $V_P$ ,  $V_S$ ,  $\rho$ ) depth by depth, at two specific depths shown by the red horizontal lines on the well-log plots. The subplots on the right compare the posterior

distributions of rock properties with prior and measured values from well logs. The orange curves are posterior distributions, the blue curves are prior distributions, and the red vertical lines are measured values from well logs.

The inversion results for Theia-1 and Cyrene-1 are presented in Figure 19. The results show that porosity, the volume fraction of kerogen, and the volume fraction of illite can be well estimated compared to the well-log measurements, while the remaining volume fractions of mineral compositions are less accurately estimated. This outcome is consistent with the sensitivity analysis, which suggests that parameters with higher sensitivity are more accurately estimated, whereas those with lower sensitivity are more difficult to constrain.

The accepted ( $V_p$ ,  $V_s$ ,  $\rho$ ) are shown in Figure 20. The range of accepted  $\rho$  is very narrow, whereas the range of  $V_p$  and  $V_s$  are broader. This is because the weight assigned to  $\rho$  is significantly higher than the weights of  $V_p$  and  $V_s$ . More specifically, the modelling error for  $\rho$  is much smaller than for  $V_p$  and  $V_s$ .

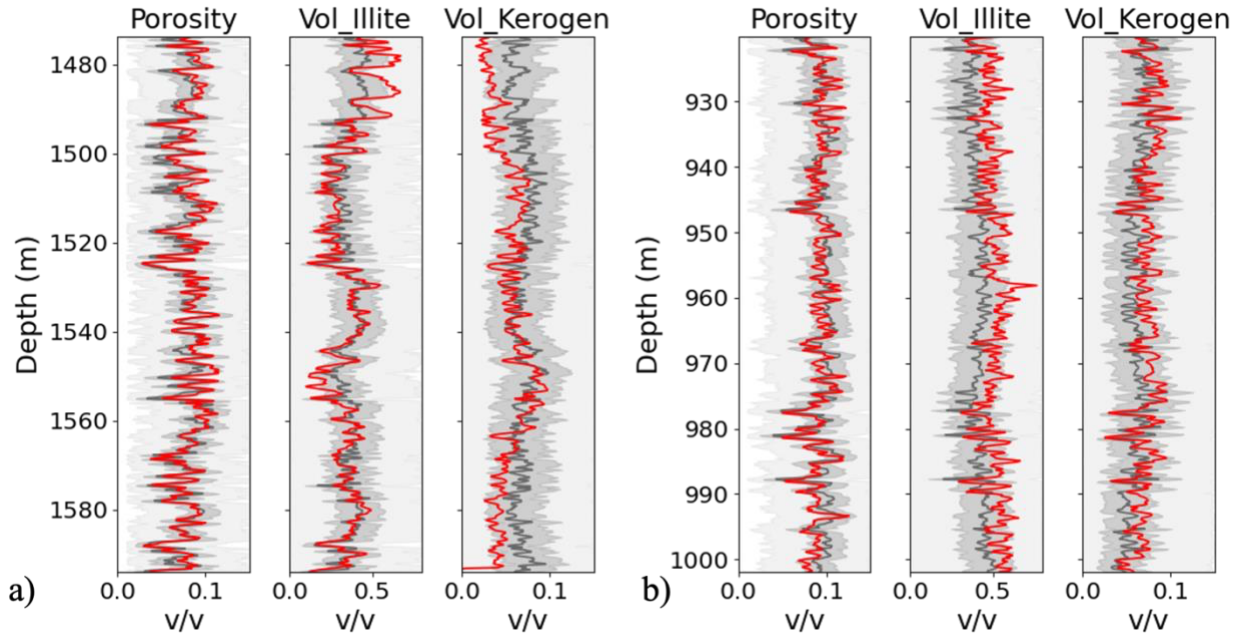


Figure 19. Inverted porosity, volume fraction of illite, volume fractions of kerogen from well-log elastic properties. a) inversion results of Theia-1 well. b) inversion results of Cyrene-1 well. The light grey areas are the ranges between minimum and maximum of the accepted samples. The dark grey areas are the ranges between 25th and 75th percentile of the accepted samples. The dark grey curves are the medians of the accepted samples. The red curves are the measured values from well logs.



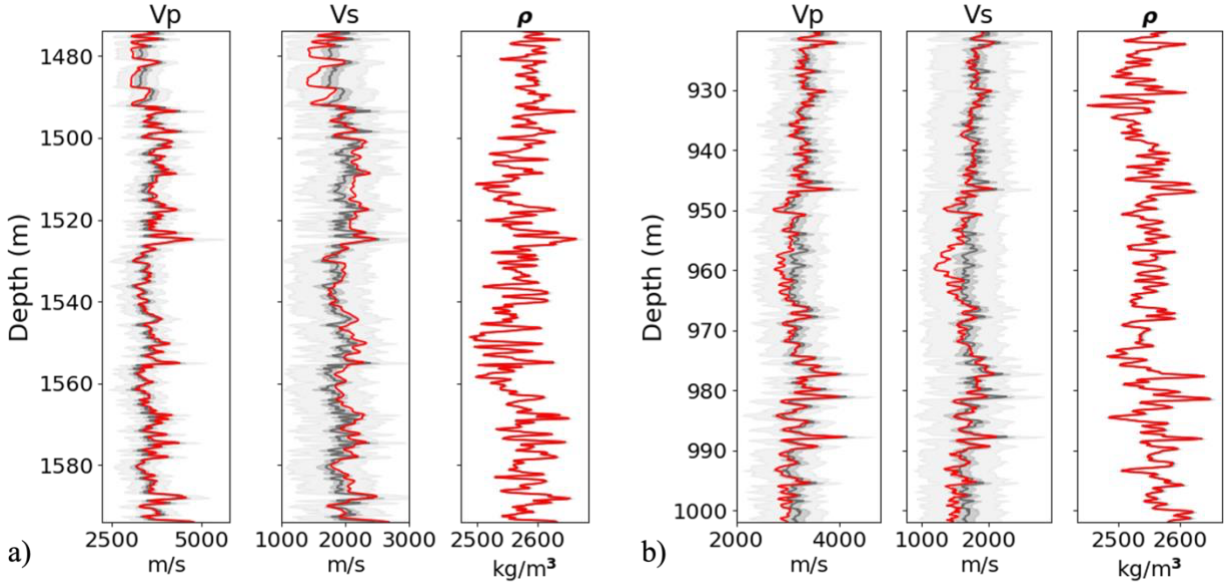


Figure 20. Accepted ( $V_p$ ,  $V_s$ ,  $\rho$ ) using ABC. a) accepted samples from Theia-1. b) accepted samples from Cyrene-1. The light grey areas are the ranges between minimum and maximum of the accepted samples. The dark grey areas are the ranges between 25<sup>th</sup> and 75<sup>th</sup> percentile of the accepted samples. The dark grey curves are the medians of the accepted samples. The red curves are the measured values from well logs.

## 5.6 Rock physics model inversion using seismic data

The same workflow of ABC is applied to invert the source rock properties from 2D ( $V_p$ ,  $V_s$ ,  $\rho$ ) sections obtained from seismic inversion. The rock physics inversion is performed point by point across the 2D sections. The means and interquartile ranges (IQR) of the inverted properties are presented in Figure 21. For porosity, the results indicate that the mean values are higher in the deeper areas of the Goldwyer III formation, with the IQR remaining relatively uniform throughout the formation. For the volume fraction of illite, the mean and IQR are higher in the deeper and shallower areas of the formation. For the volume fraction of kerogen, the mean is higher in the shallower and middle areas of the formation, and the IQR remains relatively uniform across the entire formation. The inversion results can be used to identify sweet spots with high unconventional source rock potentials.

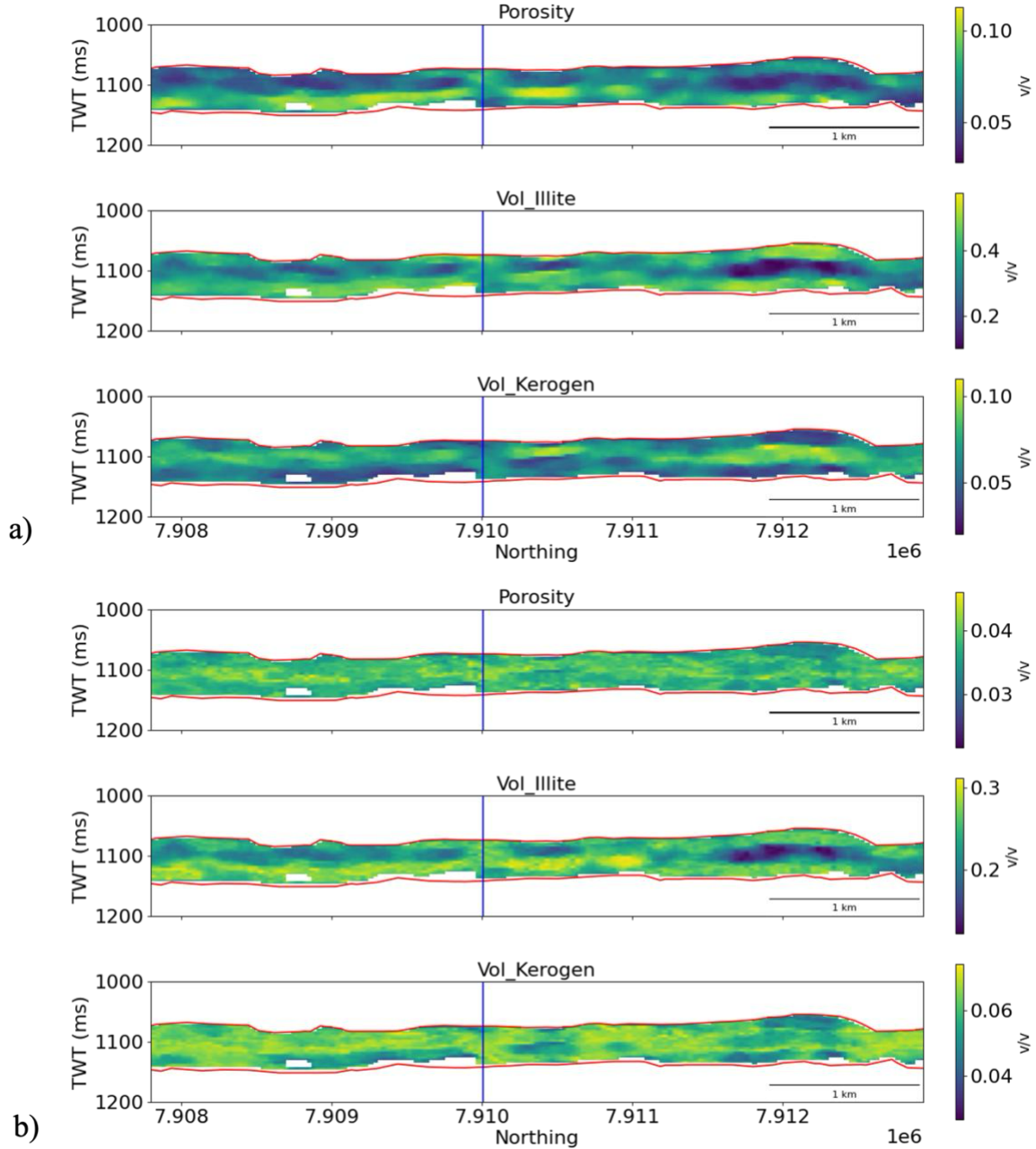


Figure 21. Means and IQRs of the accepted porosity, volume fraction of illite, and volume fraction of kerogen. The blue lines are the Theia-1 well. a) Means. b) IQRs.

## 6. Conclusion

In this study, we present a statistical rock physics inversion workflow for efficiently estimating source rock properties and quantifying their uncertainty using well logs and seismic signatures. The elastic properties of kerogen and clay minerals, such as illite and chlorite, are not well known and are therefore treated as uncertain parameters. To address this, we propose a Monte Carlo rock physics calibration approach to refine these uncertain parameters. Additionally, the pore aspect



ratio is modeled as a variable that varies with depth rather than a fixed constant, allowing for a more accurate representation of pore structure in rock physics modeling.

We introduce Weighted Approximate Bayesian Computation (ABC) to incorporate prior information from petrophysical knowledge, rock physics model calibration errors, and measured elastic property data from well logs and seismic data, enabling efficient estimation of the posterior distributions of source rock properties. Sensitivity analysis of the rock physics model provides insights into how well each input variable can be estimated through the inversion process.

The workflow is applied to a field dataset from the Canning basin. The study using well-log data demonstrates that highly sensitive inputs, such as porosity, illite, and kerogen, undergo significant updates in their posterior distributions, whereas other inputs, such as fluid properties, remain poorly constrained. The inversion workflow is validated using well-log data before being applied to seismic signatures to estimate the 2D distributions of rock properties.

There are several limitations in the proposed workflow. Firstly, only the posteriors of the top sensitive variables can be updated significantly through the rock physics inversion, while insensitive but important parameters, such as thermal maturity and fluid saturations, have limited updates in the posteriors. Second, the rock physics inversion is sensitive to the prior distributions of input variables. Therefore, accurate estimation of the prior in the study area is crucial; otherwise, it may lead to inaccurate results. Third, sensitive properties like kerogen bulk and shear moduli may vary under different conditions, such as depth and temperature. Consequently, if the rock physics model is calibrated using well logs from a specific formation and then applied to the same formation but at a much different depth in other wells, it may lead to inaccurate results.

To improve the proposed workflow, several approaches can be considered. Firstly, sensitivity analysis can be applied to investigate the sensitivity of elastic properties to source rock properties from well logs. This would help us understand why there are limited updates in some property posteriors, and whether this is due to data limitations or model limitations. Second, for properties with few updates in the posteriors, basin modeling can be applied again to incorporate the rock physics inversion results, along with basin history and boundary conditions, to further constrain the source rock properties like thermal maturity. Third, more sophisticated kerogen property model and clay mineral property model can be integrated into the workflow to address changes in properties under different conditions, making the rock physics model more practical and accurate.

## **Acknowledgement**

This work is supported by the funding from the sponsors of the Stanford Center for Earth Resources Forecasting (SCERF) and Stanford Natural Gas Initiative (NGI). We thank Partha Pratim Mandal from Qeye, Western Australia's Department of Mines, Industry Regulations and Safety for providing the necessary data used in this study. We would also like to acknowledge Lukman Mobolaji Johnson from University of Ilorin for his thoughtful discussion.

## **References**

Al Ibrahim, M. A., Mukerji, T., & Scheirer, A. H. (2020, February). A thermal-maturation dependent elastic rock physics template for organic-rich mudrocks: Construction and application. In *Fifth EAGE workshop on rock physics* (Vol. 2020, No. 1, pp. 1-5). European Association of Geoscientists & Engineers.

Alshakhs, M., & Rezaee, R. (2019). Sweet-spot mapping through formation evaluation and property modelling using data from the Goldwyer Formation of the Barrow Terrace, Canning Basin. *Petroleum*, 5(1), 13-29.

Backus, G. E. (1962). Long-wave elastic anisotropy produced by horizontal layering. *Journal of Geophysical Research*, 67(11), 4427-4440.

Batzle, M., & Wang, Z. (1992). Seismic properties of pore fluids. *Geophysics*, 57(11), 1396-1408.

Beaumont, M. A. (2010). Approximate Bayesian computation in evolution and ecology. *Annual review of ecology, evolution, and systematics*, 41(1), 379-406.

Beaumont, M. A., Zhang, W., & Balding, D. J. (2002). Approximate Bayesian computation in population genetics. *Genetics*, 162(4), 2025-2035.

Berryman, J. G. (1995). Mixture theories for rock properties, in *Rock Physics and Phase Relations: A Handbook of physical constants*, ed. T. J., Ahrens, AGU, Washington D. C., 205-228.

Bosch, M., Mukerji, T., & Gonzalez, E. F. (2010). Seismic inversion for reservoir properties combining statistical rock physics and geostatistics: A review. *Geophysics*, 75(5), 75A165-75A176.

Carmichael, R. S. (2017). *Practical handbook of physical properties of rocks and minerals (1988)*. CRC press.

Clarkson, C. R. (2013). Production data analysis of unconventional gas wells: Review of theory and best practices. *International Journal of Coal Geology*, 109, 101-146.

Eggbowaye, E. I. (2017). Petroleum source-rock evaluation and hydrocarbon potential in Montney Formation unconventional reservoir, northeastern British Columbia, Canada. *Natural Resources*, 8(11), 716.

Fenwick, D., Scheidt, C., & Caers, J. (2014). Quantifying asymmetric parameter interactions in sensitivity analysis: application to reservoir modeling. *Mathematical Geosciences*, 46, 493-511.

Finder Exploration. (2018). Maturity and unconventional resource modelling: April 2018 update for Finder Exploration's Pan-Canning Goldwyer unconventional limit project (PC-GULP) [PowerPoint slides]. Finder Exploration. (<https://wapims.dmp.wa.gov.au/WAPIMS/>)

- Foster, C. B., O'Brien, G. W., & Watson, S. T. (1986). Hydrocarbon source potential of the Goldwyer Formation, Barbwire terrace, Canning basin, western Australia. *The APPEA Journal*, 26(1), 142-155.
- Gassmann, F. (1951). Über die elastizität poroser medien. *Vierteljahrsschrift der Naturforschenden Gesellschaft in Zurich*, 96, 1-23.
- Grana, D., Azevedo, L., De Figueiredo, L., Connolly, P., & Mukerji, T. (2022). Probabilistic inversion of seismic data for reservoir petrophysical characterization: Review and examples. *Geophysics*, 87(5), M199-M216.
- Guo, Q., Ba, J., Luo, C., & Pang, M. (2021). Seismic rock physics inversion with varying pore aspect ratio in tight sandstone reservoirs. *Journal of Petroleum Science and Engineering*, 207, 109131.
- Hedan, S., Hubert, F., Prêt, D., Ferrage, E., Valle, V., & Cosenza, P. (2015). Measurement of the elastic properties of swelling clay minerals using the digital image correlation method on a single macroscopic crystal. *Applied Clay Science*, 116, 248-256.
- Hertz, H. (1882). Ueber die Berührung fester elastischer Körper.
- Humbert, P. (1972). Propriétés élastiques de carbonates rhomboédriques monocristallins: Calcite, magnésite, dolomite. *Comptes Rendus de l'Académie des Sciences Paris*, 275, 391.
- Iqbal, M. A., Rezaee, R., Laukamp, C., Pejčić, B., & Smith, G. (2022). Integrated sedimentary and high-resolution mineralogical characterisation of Ordovician shale from Canning Basin, Western Australia: Implications for facies heterogeneity evaluation. *Journal of Petroleum Science and Engineering*, 208, 109347.
- Kashinath\*, A., Szulczewski, M. L., & Dogru, A. H. (2019, October). Modeling the effect of maturity on the elastic moduli of kerogen using atomistic simulations. In *Unconventional Resources Technology Conference, Denver, Colorado, 22-24 July 2019* (pp. 391-406). Unconventional Resources Technology Conference (URTeC); Society of Exploration Geophysicists.
- Mavko, G., Mukerji, T., & Dvorkin, J. (2020). *The rock physics handbook*. Cambridge university press.
- Mindlin, R. D. (1949). Compliance of elastic bodies in contact. *Journal of Applied Mechanics*, 16, 259–268.
- Minter, A., & Retkute, R. (2019). Approximate Bayesian Computation for infectious disease modelling. *Epidemics*, 29, 100368.
- Mondol, N. H., Jahren, J., Bjørlykke, K., & Brevik, I. (2008). Elastic properties of clay minerals. *The Leading Edge*, 27(6), 758-770.

Mukerji, T., Avseth, P., Mavko, G., Takahashi, I., & González, E. F. (2001). Statistical rock physics: Combining rock physics, information theory, and geostatistics to reduce uncertainty in seismic reservoir characterization. *The Leading Edge*, 20(3), 313-319.

Park, J., Yang, G., Satija, A., Scheidt, C., & Caers, J. (2016). DGSA: A Matlab toolbox for distance-based generalized sensitivity analysis of geoscientific computer experiments. *Computers & geosciences*, 97, 15-29.

Peters, K. E., Schenk, O., Hosford Scheirer, A., Wygrala, B., & Hantschel, T. (2017). *Basin and petroleum system modeling* (pp. 381-417). Springer International Publishing.

Rousseeuw, P. J. (1984). Least median of squares regression. *Journal of the American statistical association*, 79(388), 871-880.

Rubin, D. B. (1984). Bayesianly justifiable and relevant frequency calculations for the applied statistician. *The Annals of Statistics*, 1151-1172.

Scheidt, C., Li, L., & Caers, J. (Eds.). (2018). *Quantifying uncertainty in subsurface systems*. John Wiley & Sons.

Simmons, G. (1965). Single crystal elastic constants and calculated aggregate properties. *Journal of the Graduate Research Center*, 34(1), 1.

Sunnåker, M., Busetto, A. G., Numminen, E., Corander, J., Foll, M., & Dessimoz, C. (2013). Approximate bayesian computation. *PLoS computational biology*, 9(1), e1002803.

U.S. Energy Information Administration (2015). Technically Recoverable Shale Oil and Shale Gas Resources: Australia, 2015.  
( [https://www.eia.gov/analysis/studies/worldshalegas/pdf/australia\\_2013.pdf](https://www.eia.gov/analysis/studies/worldshalegas/pdf/australia_2013.pdf))

van Hattum, J., Bond, A., Jablonski, D., & Taylor-Walshe, R. (2019). Exploration of an unconventional petroleum resource through extensive core analysis and basin geology interpretation utilising play element methodology: the Lower Goldwyer Formation, onshore Canning Basin, Western Australia. *The APPEA Journal*, 59(1), 464-481.

Vernik, L., & Landis, C. (1996). Elastic anisotropy of source rocks: Implications for hydrocarbon generation and primary Migration1. *AAPG bulletin*, 80(4), 531-544.

Wang, Z., Wang, H., & Cates, M. E. (2001). Effective elastic properties of solid clays. *Geophysics*, 66(2), 428-440.

Whitaker, M. L., Liu, W., Wang, L., & Li, B. (2010). Acoustic velocities and elastic properties of pyrite (FeS<sub>2</sub>) to 9.6 GPa. *Journal of Earth Science*, 21, 792-800.

Wu, T., & Firoozabadi, A. (2020). Mechanical properties and failure envelope of kerogen matrix by molecular dynamics simulations. *The Journal of Physical Chemistry C*, 124(4), 2289-2294.